Supporting Information

for

A Bipolar Electrochemical Approach to Constructive Lithography: Metal/Monolayer Patterns via Consecutive Site-Defined Oxidation and Reduction

Assaf Zeira,[†] Jonathan Berson, [†] Isai Feldman, [‡] Rivka Maoz[*,†] and Jacob Sagiv[*,†]

Departments of Materials and Interfaces and Chemical Research Support,
The Weizmann Institute of Science, Rehovot 76100, Israel

[†] Department of Materials and Interfaces.

[‡] Department of Chemical Research Support.

[*]Corresponding authors. E-mail:
jacob.sagiv@weizmann.ac.il ; rivka.maoz@weizmann.ac.il

Preliminary CEP–CET Experiments: Examining the Effects of Variable Voltage Bias and Length of Time the Voltage Bias is Applied in Each Step of the Process

The results summarized in Figure S1 point to the high sensitivity of both the CEP and CET steps to the magnitude of the applied voltage bias and the time the voltage bias is applied, which clearly demonstrates the electrochemical nature of the transformations responsible for both the pattern printing on the target monolayer (CEP) and the subsequent transfer of the metal to the printed pattern (CET).

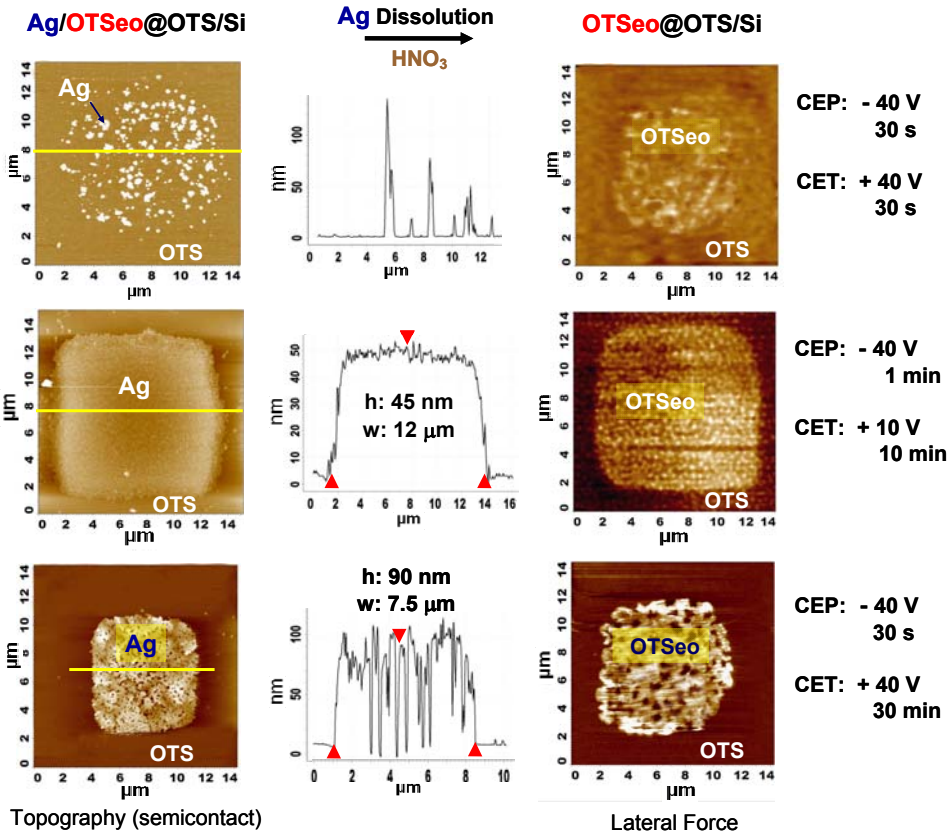

Figure S1. Examples of SFM images of transferred silver features and monolayer prints under the transferred metal obtained in experiments performed under different conditions with respect to the voltage bias and length of time the voltage bias was applied in each step of the CEP–CET process (the voltage sign refers to the polarity of the STAMP – see Figure 1, paper). All STAMP patterns used here were prepared identically to that shown in Figure S5 below, and in all experiments the ambient humidity was close to 100% RH, the STAMP-TARGET sandwich being exposed to the humid atmosphere for 20 min before the application of the bias voltage. The left and middle columns show representative topographic images (semicontact mode) of a transferred silver square (TARGETeo) and height-width profiles along the respective marked lines. The right column shows lateral force images (contact mode) of monolayer prints obtained after removal of the silver from the respective metallized

specimens (as in Figure 2, paper). It should be noted that the middle row images were obtained from metallized and metal-free TARGETeo squares of the pattern also displayed in Figures S5 and S6 below.

With equal high voltages and short times in both steps (top row), the pattern printing as well as the transfer of the metal are partial, resulting in small separated OTSeo islands on which discrete metal particles are formed, with heights ranging from a few nanometers to ca 120 nm (i.e. almost three times the average thickness of a compact transferred film produced with a stamp of the same kind (middle row)). With equal high voltages but short CEP time and very long CET time (bottom row), the pattern printing is partial as before, while the initially transferred metal grains continue to grow via a metal-on-metal deposition mechanism that results in a uniform "sponge-cake" film morphology with voids spanning the entire film. Finally, with high voltage and moderate CEP time, and significantly lower voltage and longer CET time (middle row), a rather smooth, compact metal film is obtained. A close inspection of the monolayer print produced under these conditions (right column, middle row) reveals a nanometrically resolved grainy structure of the OTSeo image, which might reflect the positions and sizes of the stamp metal grains initially touching the target monolayer during the CEP step.

Topographic Artifact in the Contact Mode Imaging of OTSeo@OTS/Si Patterns

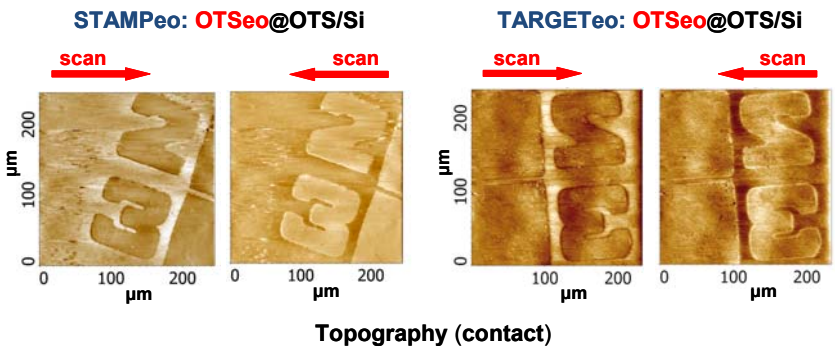

Figure S2. Example of inverted height contrast in the contact mode imaging of printed OTSeo@OTS/Si monolayer patterns (same patterns as in Figure 2, paper), depending on the direction of tip motion; left to right (→) vs right to left (←).

Figure S2 shows printed OTSeo features from the STAMPeo and TARGETeo patterns displayed in Figure 2 (paper) that appear with inverted height contrast relative to the unmodified OTS background when the tip motion in the horizontal scan is from right to left as compared with that from left to right (as displayed in Figure 2, paper). This imaging artifact, caused by "crosstalk" between torsion and vertical bending of the cantilever when scanned over a heterogeneous surface exposing both hydrophilic (high friction) and hydrophobic (low friction) regions,[1-5] is a characteristic feature of the nondestructive OTS patterning in constructive lithography.

Photochemical Assessment of the Porous Structure of the Granular Silver Films Employed as Stamps in the Present CEP–CET Experiments

The experiments summarized in Figures S3 and S4 were performed under the assumption that the optical semitransparency of granular silver films of the kind employed as stamps in the present CEP–CET experiments has mainly to do with passage of the light through pores in the metal film; either directly, through pores spanning the entire film, or via multiple reflections within networks of interconnected pores that provide longer but nevertheless continuous paths connecting the outer surface of the metal film to the film–OTS interface. As UV-induced photocleavage is routinely employed by us in the patterning of OTS/Si monolayers,[4,5] this assumption implies that a porous silver film deposited by evaporation on the monolayer should behave very much like a contact mask used in the photocleavage-based patterning of such monolayers,[4] patterns produced in this manner providing an image of the pores through which the radiation could reach the OTS monolayer through the metal film (Figure S3). Sub-wavelength monolayer photopatterning with such thin metal film masks should be possible as the result of a near-field effect,[6] considering the close proximity of the evaporated metal film to the patterned monolayer.

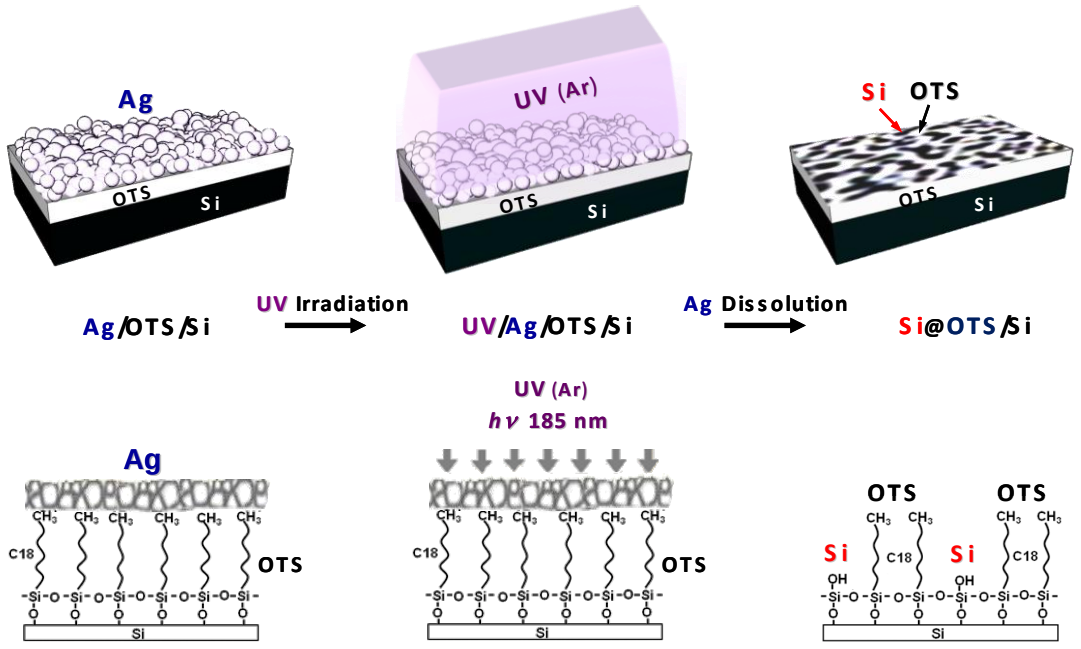

Figure S3. Schematic representation of the photocleavage-based patterning of a OTS/Si monolayer with UV irradiation passing through a granular silver film deposited on the monolayer. The resulting pattern (Si@OTS/Si) is expected to consist of bare silicon regions (Si), produced by the cleavage of monolayer hydrocarbon tails (see molecular schemes in the bottom row) by light reaching these regions through pores in the silver film, surrounded by the unaffected monolayer background (OTS/Si). The UV irradiation was performed as described before.[4]

The average grain size and corrugation of the as-prepared 40 nm silver film in Figure S4-A are seen to be significantly larger than those of the 80 nm film (compare **a** and **b**), which indicates that the thicker film is also denser and so less porous and less transparent to light compared to the thin film. Upon irradiation, the corrugation of the 40 nm film increases considerably, while this effect is barely noticeable in the identically irradiated 80 nm film (compare images **c** and **a** with **d** and **b**, Figure S4-A). Thus the structural change of the 40 nm silver film following irradiation may not be ascribed to a direct effect of the interaction of the UV light with the silver, but rather to the expected radiation-induced damage of the underlying OTS monolayer, which leads to a structural reorganization of the metal film residing on top of it. Since the thin silver film is more transparent than the thicker one, the damage caused to the OTS monolayer under it is more pronounced and so the structural modifications associated with it. This scenario is fully corroborated by the experimental results summarized in Figure S4-B.

Images **e** in Figure S4-B are representative of a defect-free hydrophobic OTS/Si monolayer. The respective water condensation image shows nanoscale water droplets (the dark dots) that start nucleating randomly over the entire monolayer surface as the ambient humidity reaches saturation (100% RH). Images **f** and **g** show water condensation patterns very different from that formed on the pristine OTS monolayer (**e**), and also different from one another. A clear correlation can be found between these water patterns and the corresponding SFM images.

Most strikingly, images **f** (obtained after removal of the 40 nm silver film from the irradiated specimen) show a mottled surface structure in which intact OTS patches (with heights of ~2.5 nm[2,4,5]) are separated by bare silicon regions, both of which being easily identified by SFM due to the positive and respectively negative contrast of the OTS features in the respective topographic and lateral force images.[5] The distribution of hydrophobic (OTS) and hydrophilic (bare Si) features in the SFM images is seen to be well reproduced in the water condensation pattern, the dark patches (water) following here (as in the respective topographic SFM image) the underlying hydrophilic pattern of bare silicon. In images **g** (obtained after removal of the 80 nm silver film from the irradiated specimen), the SFM tip apparently cannot penetrate to the bottom of the tiny holes in the OTS monolayer produced by the irradiation. These holes are however revealed by the water condensation pattern due to the fact that nanoscale water droplets nucleating at such hydrophilic sites in the monolayer tend to grow under prolonged exposure to a water saturated atmosphere while remaining pinned to their isolated nucleation sites on the otherwise hydrophobic monolayer surface.

We may thus conclude that the mottled morphology of the irradiated monolayer evident in Figure S4-B, images **f**, in which intact monolayer patches alternate with bare silicon regions, confirms our assumption that UV light passing through a thin granular metal film is not homogeneously attenuated, the partial transparency of the film representing the fraction of unattenuated light directly transmitted through empty pores present in the film while the rest of it is totally blocked by metal reflection and absorption. However, because the metal film morphology itself also changes in the course of the irradiation as a result of structural changes caused by the transmitted light to the underlying organic monolayer (Figure S4-A), damaged monolayer patterns such as those produced here upon prolonged irradiation of the

Ag (40 nm)/OTS/Si specimen (Figure S4-B, **f**) tend to overestimate the initial porosity of the deposited metal film.

All SFM images displayed in Figure S4 were acquired on a SOLVER P47 SFM instrument (NT-MDT) equipped with a 16 μm scanner.[2]

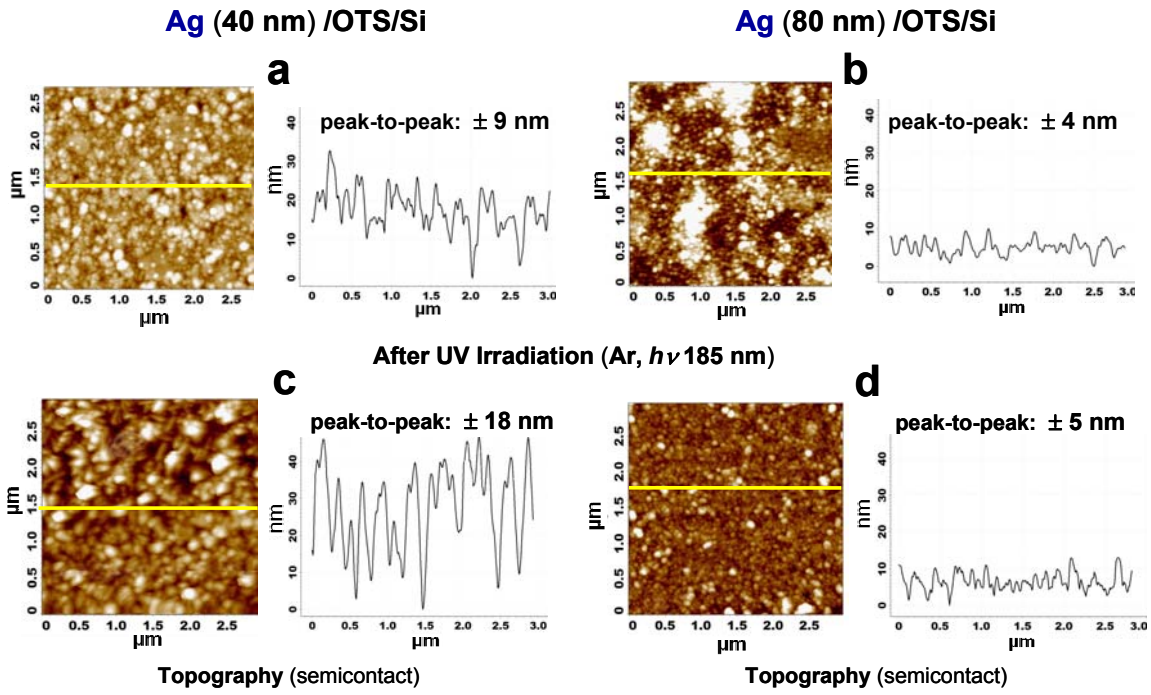

Figure S4-A. SFM images acquired from ~40 nm and ~80 nm thick silver films (Ag/OTS/Si) prepared under identical deposition conditions on identical OTS/Si monolayers (see Experimental, paper), before (**a** and **b**) and after (**c** and **d**) 3 hours of UV irradiation (according to Figure S3),[4] both specimens being equally exposed to the radiation in the UV chamber.

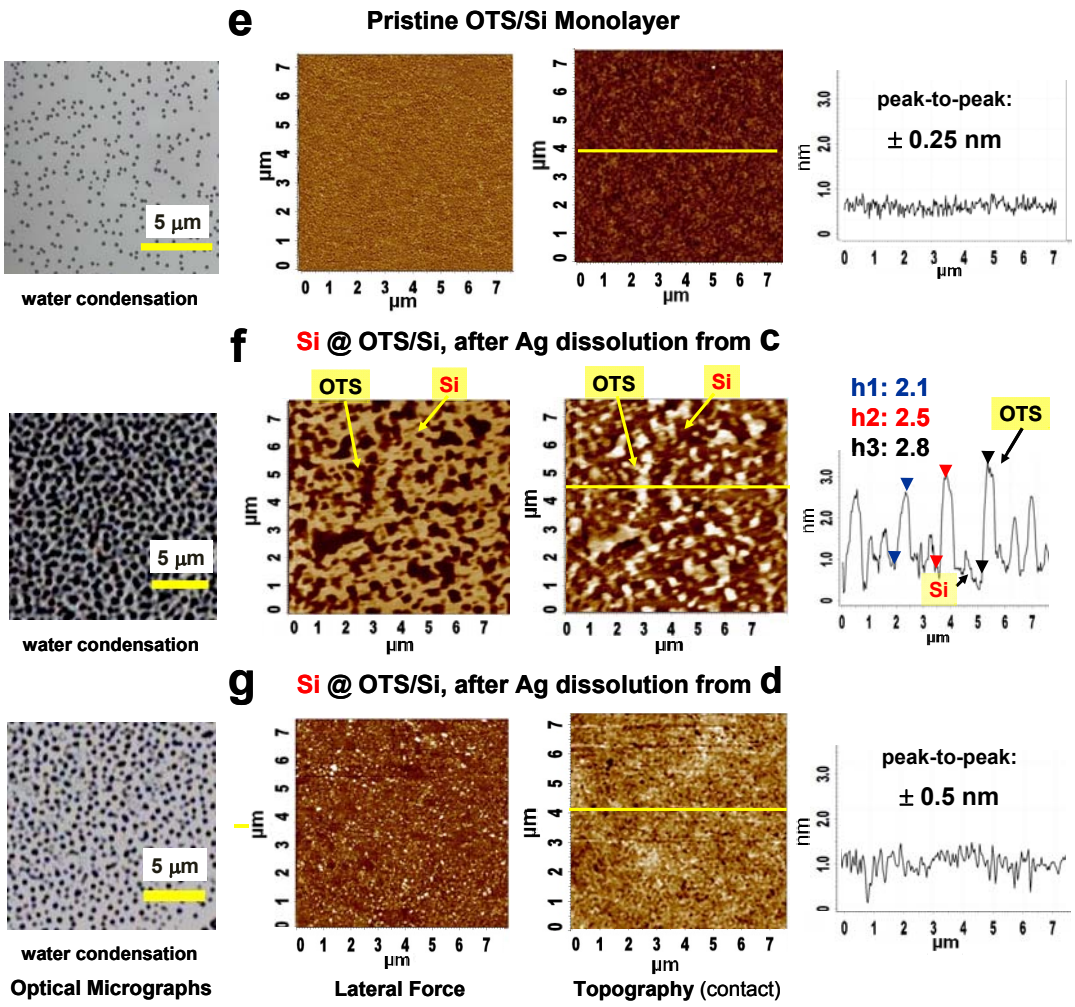

Figure S4-B. Comparative optical micrographs of water condensation patterns[4] and SFM images acquired from a pristine OTS/Si monolayer (**e**) and from the irradiated Ag/OTS/Si specimens (**c** and **d** in part **A**) after dissolution of the respective silver films in HNO_3 (**f** and **g**) (see Methods and Materials, paper). The notation Si@OTS/Si denotes bare silicon regions surrounded by the OTS/Si monolayer (Figure S3).

CET Self–Correction Effect

The pattern printing and metallization experiment in Figure S5 was performed with a Ag/OTS@OTS/Si STAMP fabricated by the evaporation of a ~40 nm thick silver film through a 1500 mesh copper grid mask covering the entire STAMP surface. According to the SFM images in the two top rows of Figure S5, the average heights of the silver squares in the STAMP pattern are much lower (~21 nm) than the

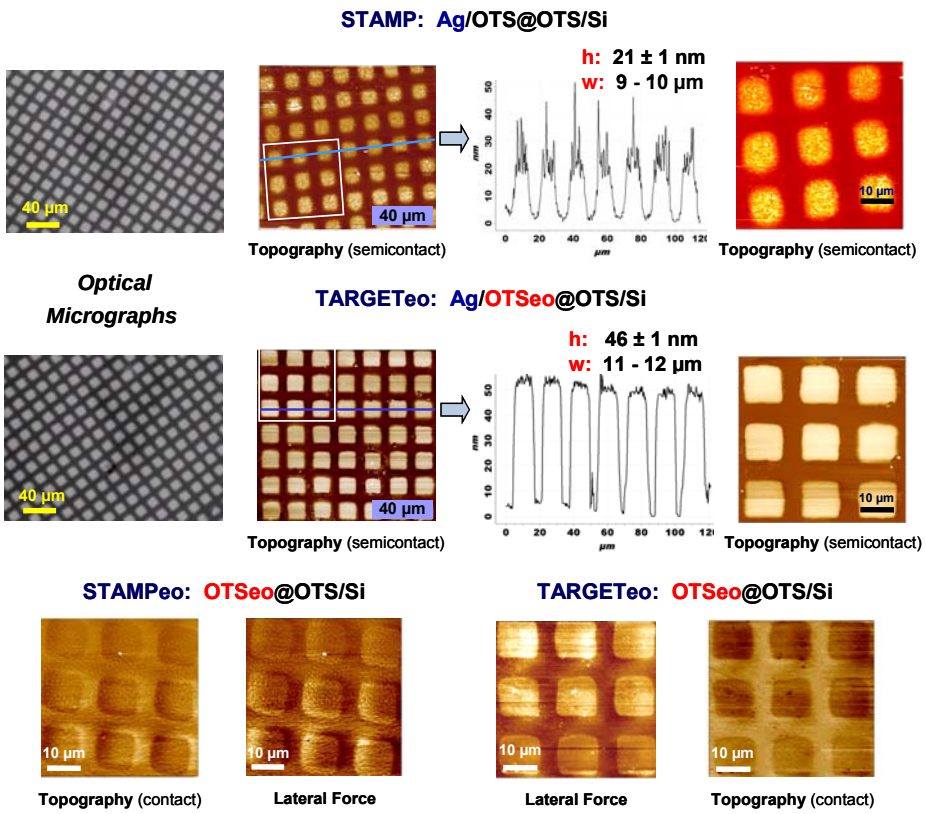

Figure S5. Example of optical micrographs, SFM images and height-width profiles obtained from selected similar regions of: (top row) Ag/OTS@OTS/Si micropattern (STAMP) produced with an SPI Fine Grid Mesh (Cu 02901C, 1500 mesh) as contact mask, and (middle row) its Ag/OTSeo@OTS/Si replica (TARGETeo) resulting from the implementation (according to Figure 1, paper) of the consecutive CEP (1) and CET (2) operations. The indicated widths (w) of the silver squares are values measured at their half heights, the indicated heights (h) being the average values of the average heights of the imaged squares along with the respective standard deviations. Bottom row: SFM images of selected similar regions of the STAMPeo and TARGETeo monolayer prints resulting from the CEP–CET process. The CEP and CET operations were performed as described in Figure 2 (paper).

nominal thickness of the evaporated silver film (ca. 40 nm), which is, however, reasonably well reproduced in the transferred TARGETeo silver features (~46 nm). Furthermore, the widths (at half height) of the silver squares in the STAMP (9 – 10 µm) are significantly smaller than those in the respective transferred squares (11 – 12 µm), while their metal grain size and surface corrugation are much larger. Compared with the STAMP, the considerably smoother and more compact appearance of the TARGETeo metal squares, as well as their larger height/width aspect ratios, clearly demonstrate that the STAMP metal pattern was not transferred mechanically, but rather via a dissolution–redeposition process that results in a different metal film morphology. But how can the transferred metal squares be both denser and taller than

those from which they were generated, and how can we explain the apparently missing material in the STAMP metal pattern?! Figure S6 provides answers to these questions.

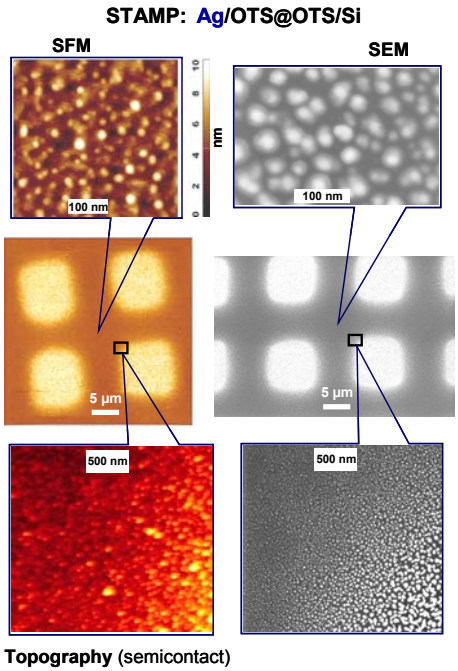

Figure S6-A. Comparative SFM and SEM (scanning electron microscope) images of several silver squares of same STAMP pattern as in Figure S5, with higher resolution zooms on border regions of the metal squares (bottom row images) and on central regions of the gaps between them (top row images).

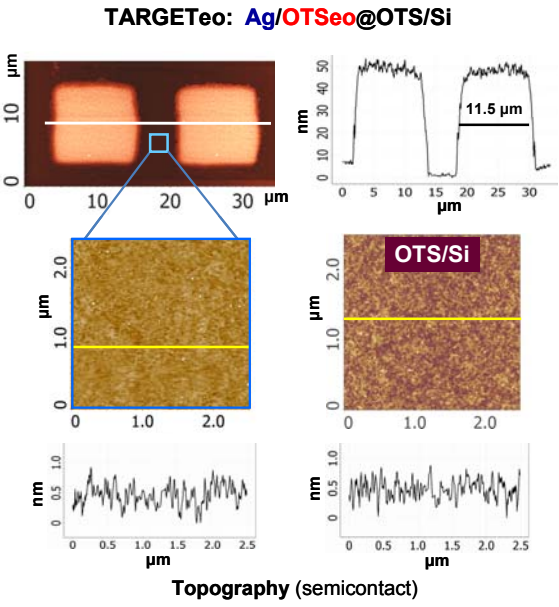

Figure S6-B. Top: SFM image of two adjacent silver squares in the TARGETeo replica pattern of the STAMP pattern shown in part **A**, and height–width profile along the marked line through the silver squares and the gap between them.

Bottom: Comparative higher resolution SFM images and corresponding height–width profiles taken from the gap region between the silver squares in the top image (left side) and from a pristine, freshly prepared OTS/Si monolayer (right side).

Apparently, the grid mesh employed as contact mask in the preparation of the STAMP for this experiment did not afford tight enough contact with the OTS surface, metal nanoparticles being thus deposited also under the bars of the grid (corresponding to the gaps between metal squares in the STAMP – Figure S6-A, top row images). The size of these nanoparticles is seen to decrease gradually on going from the open square areas of the grid toward the centers of the bars (respectively metal squares and the gaps between them in the STAMP – Figure S6-A, bottom row images). Because such small metal particles are not resolved in the large (tens of micrometers) SFM scans, the apparent SFM–determined thickness of the STAMP metal squares (Figure S5) corresponds to the height difference between the top surface of the squares and the carpet of nanoparticles covering the gap regions between them, which is obviously smaller than the nominal thickness of the evaporated metal film. Unlike the STAMP, the gaps between the silver squares in the TARGETeo replica pattern are seen to be practically free of metal particles, the surface corrugation in these OTS regions being identical to that characteristic of pristine OTS/Si monolayers (Figure S6-B), which suggests that all metal deposited on the STAMP, including the nanoparticles in the gap areas between the silver squares, was exclusively transferred to the squares of the TARGETeo pattern, thus giving rise to replica metal features slightly higher than the nominal thickness of the evaporated STAMP features.

It follows from this analysis that silver nanoparticles present in the gap areas of the STAMP pattern must have been transported laterally during the CET step to adjacent silver squares and then redeposited within the corresponding silver square regions of the TARGETeo pattern. This scenario is entirely consistent with the proposed bipolar mechanism of metal dissolution–transport–deposition in the potential gradient established within a water–soaked granular metal film (see paper). Since water is present here only as an ultrathin layer adsorbed on the metal particles (Figure 4, paper), electrochemical contact between the carpet of small nanoparticles covering the gap areas of the STAMP and the surface of the TARGET can be established only through the protruding metal film squares of the STAMP. Therefore

all transfer of information and material between STAMP and TARGET during the CEP and CET steps must take place via these metal squares, which ultimately results in the concentration of the entire metal dispersed on the STAMP surface within those regions of the TARGET that came in direct electrical contact with the protruding metal features of the STAMP. The very appealing outcome of this process is therefore an interesting and rather unusual self–correction effect that allows quite good replica patterns to be fabricated with less perfect stamps!

X-ray Diffraction Data

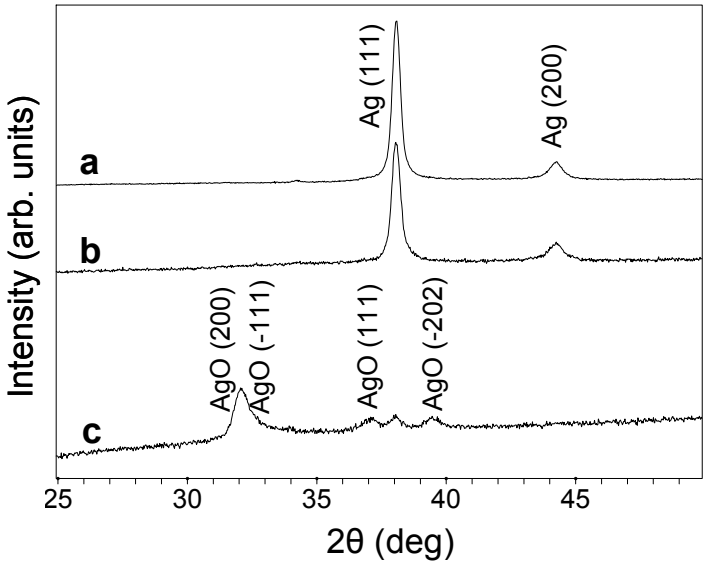

Figure S7. X–ray diffraction (XRD) spectra (2θ/θ scans) recorded from: (a) ~40 nm evaporated Ag/OTS/Si film (STAMP), (b) transferred Ag/OTSeo/Si film (TARGETeo) resulting from the application of the consecutive CEP and CET operations to a STAMP film, (c) oxidized silver film produced by the exposure of an evaporated Ag/OTS/Si film to UV-ozone in a UV cleaner equipped with Hg-vapor lamps (model NL-UV 253, NLE, Nagoya, Japan), under oxygen purge (O_2 purity 99.9999 %). The XRD curves of samples **a** and **b** show only two distinct peaks, at 37.1º and 44.3º, corresponding to the (111) and respectively (200) reflections of 3C–Ag (JCPDS file: 4-0783). Sample **c** shows several peaks of the silver oxide AgO (JCPDS file: 43-1038) and only a weak residual peak (111) of the metal silver.

References

1. Hoeppener, S.; Maoz, R.; Sagiv, J. Constructive Microlithography: Electrochemical Printing of Monolayer Template Patterns Extends Constructive Nanolithography to the Micrometer–Millimeter Dimension Range. *Nano Lett.* **2003**, *3*, 761–767.

2. Liu, S.; Maoz, R.; Sagiv, J. Planned Nanostructures of Colloidal Gold via Self-Assembly on Hierarchically Assembled Organic Bilayer Template Patterns with In-situ Generated Terminal Amino Functionality. *Nano Lett.* **2004**, *4*, 845–851.

3. Wouters, D.; Willems, R.; Hoeppener, S.; Flipse, C. F. J.; Schubert, U. S. Oxidation Conditions for Octadecyl Trichlorosilane Monolayers on Silicon: A Detailed Atomic Force Microscopy Study of the Effects of Pulse Height and Duration on the Oxidation of the Monolayer and the Underlying Si Substrate. *Adv. Funct. Mater.* **2005**, *15*, 938−944

4. Zeira, A.; Chowdhury, D.; Maoz, R.; Sagiv, J. Contact Electrochemical Replication of Hydrophilic–Hydrophobic Monolayer Patterns. *ACS Nano* **2008**, *2*, 2554–2568.

5. Zeira, A.; Chowdhury, D.; Hoeppener, S.; Liu, S.; Berson, J.; Cohen, S. R.; Maoz, R.; Sagiv, J. Patterned Organosilane Monolayers as Lyophobic-Lyophilic Guiding Templates in Surface Self-Assembly: Monolayer Self-Assembly versus Wetting Driven Self-Assembly. *Langmuir* **2009**, *25*, 13984–14001.

6. Sun, S.; Montague, M.; Critcheley, K.; Chen, M.-S.; Dressick, W. J.; Evans, S. D.; Leggett, G. J. Fabrication of Biological Nanostructures by Scanning Near-Field Photolithography of Chloromethylphenylsiloxane Monolayers. *Nano Lett.* **2006**, *6*, 29–33.